Journal of MATERIALS RESEARCH

Article
DOI: 10.1557/jmr.2020.100

Microstructural characterization of phase-separated co-deposited Cu–Ta immiscible alloy thin films

Max Powers[1,a)], Benjamin Derby[1], Alex Shaw[1], Evan Raeker[1], Amit Misra[1]

[1]*Department of Materials Science and Engineering, University of Michigan, Ann Arbor, Michigan 48109, USA*

[a)]Address all correspondence to this author. e-mail: maxpow@umich.edu

Received: 7 January 2020; accepted: 7 April 2020

Elevated temperature co-sputtering of immiscible elements results in a variety of self-organized morphologies due to phase separation. Cu–Ta is used as a model system to understand the evolution of phase-separated microstructural morphologies by co-sputtering thin films with nominal 50–50 at.% composition at four temperatures: 25, 400, 600, and 800 °C. Scanning/transmission electron microscopy of the film cross sections showed the microstructure morphology varied from nanocrystalline Cu–Ta at 25 °C to a wavy ribbon-like structure at 400 °C, to Cu-rich agglomerates surrounded by Ta-rich veins at 600 and 800 °C. In the agglomerate-vein morphology, microstructural features were present on two length scales, from a few nanometers to a few tens of nanometers, thus making the structures hierarchical. On the nanoscale, the Cu-rich agglomerates contained Ta precipitates, whereas the Ta-rich veins had embedded Cu nanocrystals. The various microstructures can be attributed to the highly disparate constituent element interdiffusion at the deposition temperatures with the Cu having orders of magnitude higher mobility than Ta at the deposition temperatures. This study of processing–microstructure relationship will be useful in guiding the design of hierarchical multiphase microstructures in binary or multicomponent thin films with tailored mechanical properties.

Introduction

Immiscible metal alloy systems are subject to phase-separating driving forces that can induce chemically sharp interfaces between the constituent elemental regions. What makes these systems unique is the processing tunability of the microstructure morphologies to obtain desired mechanical or chemical properties. Cu-X [where X is a body-centered cubic (BCC) group V or VI transition metal] alloys are model systems of binary alloys that are nearly completely immiscible across a large range of processing temperatures which results in the self-assembly of phase-separated regions of pure face-centered cubic (FCC) and BCC phases. In addition, the systems Cu–Nb [1], Cu–Cr [2], Cu–Mo [3], and Cu–W [4], typically in nanolaminate morphologies, have all shown prominent bulk mechanical or nanomechanical performance that is affiliated with microstructural heterogeneities [5]. Past research shows these systems can have high flow strengths [6], improved radiation tolerance [7], and prominent fatigue resistance [8]. Furthermore, this enhanced performance is related to the length scale of phase-separated regions, which dictates the dominant plastic deformation mechanism as interface–dislocation interactions become key considerations for mechanical behavior [9]. Interface–dislocation interactions include dislocation pile-up, confined layer slip, deformation twinning, and dislocation climb, all of which were observed at various points during compressive loading of Cu–Mo [3] and Cu–Ag nanocomposites [5]. With specific processing conditions, the Cu–X alloys will form nanolaminate or bicontinuous intertwined structures with yield strengths an order of magnitude greater than annealed bulk samples. As these properties are based on microstructure morphology, an increased understanding of the processing–microstructure relationship will enable design of interfacial microstructures in phase-separated thin films for tailored mechanical and physical properties.

Physical vapor deposition (PVD) offers a variety of tunable processing parameters including deposition temperature, substrate selection, depositing sequence, target power variations, and deposition rate. Scientists can elucidate the processing–microstructure relationship by varying these deposition conditions to control the thermodynamics and kinetics of the

sputtered metal atoms (adatoms) as they land on the surface of the substrate. Fundamental work affiliating metallic film microstructure with the processing parameters can be found in the Thornton zone diagram [10]. The Thornton zone diagram gives a preliminary understanding of film growth and microstructures for monolithic systems and certain sequentially deposited binary systems, but co-deposited binary systems are yet to be fully explored. The phase-separating driving force of immiscible metal alloys paired with complex phase-ordering kinetics of thin film deposition leads to a range of novel self-assembled morphologies. This opens the door on a variety of model Cu–X systems, such as Cu–Ta that is the focus of this article.

Before delving into Cu–Ta, it is pertinent to review the reported phase-separated morphologies in another FCC–BCC system, Cu–Mo. As reported for co-deposited Cu–Mo films [11, 12], Cu-rich and Mo-rich regions organized into metastable architectures of concentration modulations with orientations controlled by deposition temperature. These modulations are the result of a delicate interplay between the rate of phase separation and the rate of deposition. The rate of phase separation is abetted by surface diffusion and the kinetic energy of the landing adatoms. The adatoms will diffuse a specific distance on the surface before being buried by the oncoming deposition layer. Therefore, altering the deposition rate will either permit or arrest full phase separation and give rise to lateral, vertical, or randomly oriented composition modulations [13]. The phase-separating behavior and influence of kinetics in the formation of these modulations have been verified experimentally as well as computationally with phase-field mesoscale modeling [14]. Interestingly, some of the modulations contained hierarchical structures with Cu- and Mo-rich regions organizing themselves as metastable states on multiple length scales (nano and micro). The definition of a hierarchical structure is a morphology that has distinct features on a specific length scale and a separate set of features on another length scale. Explaining these hierarchical structures requires consideration of the adatoms' relative mobilities. While depositing at elevated temperatures, the mobility of Cu adatoms is orders of magnitude greater than that of Mo adatoms. The resultant calculated surface diffusion length of Cu is significantly larger than Mo, which gave rise to a bimodal architecture as phase-rich regions separated on two length scales with large Cu and Mo regions containing embedded Cu and Mo minority clusters stabilized as metastable phases [12]. The hierarchical structures are of particular nanomechanical interest as the minority element clusters in a phase-separated region may behave as precipitates in a matrix. Given the limited experimental data reported on Cu–Mo, fundamental understanding of the mechanisms of self-organized morphologies in co-deposited immiscible systems is still evolving and characterization of other systems is crucial to generalize the trends. The Cu–Ta system is well-studied in the semiconductor industry [15] but could have promising nanomechanical applications as evidenced by the high strength of the similar Cu–Nb system [1]. The mismatch between the lattice parameters, melting temperatures, elastic moduli, and inter-diffusion coefficients between the FCC and BCC elements in systems such as Cu–Mo, Cu–Nb, and Cu–Ta are widely different [16]. There is a paucity of data on the processing–microstructure relationship of Cu–Ta co-deposited at elevated temperatures and specifically how heterogeneities in the structure will form as the structure self-assembles. In addition, Cu and Ta have highly disparate mobilities at elevated temperatures and with PVD co-deposition may form hierarchical structures akin to those seen for Cu–Mo. Any bicontinuous or modulated structures present in co-deposited Cu–Ta could be advantageous for mechanical performance as they have a higher interface volume fraction and a third dimensionality for interface–dislocation interactions (as opposed to two dimensions for interface–dislocation interaction in nanolaminate multilayer systems), which may suppress shear localization or trap gliding dislocations [17].

Previous work on Cu–Ta co-sputtered at room temperature shows that the as-deposited structure will vary with respect to alloy composition [18]. Muller et al. reported that across all compositions, Cu tends to form into a FCC structure, whereas Ta will form into either BCC also noted as α-Ta, or tetragonal, specified as the β-uranium structure, or as β-Ta, which is a metastable state. In a second work, Muller et al. focused on an as-deposited Cu–34 at.% Ta to deduce the formation mechanism of α or β-Ta [19]. The as-deposited film formed nanocrystalline Cu–Ta grains arranged in a superlattice. Upon annealing at 400 and later 600 °C, Cu coalesced into clusters inside a β-Ta matrix via spinodal decomposition as proven by signs of "uphill" diffusion in tomographic imaging.

The orientation relationship between phase-separated regions provides critical information on the interface character and its influence on mechanical behavior. However, it is difficult to ascertain meaningful orientation relationships in co-sputtered Cu–Ta because of reduced feature size and far-from-equilibrium structures. Work by Kwon et al. [20] on consecutively deposited Cu–Ta layers (with β-Ta and FCC Cu phases) depicts a heteroepitaxial relationship at the interface of $Cu_{(111)[2\bar{2}\bar{0}]} \| \beta\text{-}Ta_{(001)[3\bar{3}\bar{0}]}$ observed with electron diffraction. Other work on as-deposited Cu–Ta multilayers denotes metastable β-Ta (002) and Cu(111) preferred texture as seen in X-ray diffraction [21]. After annealing, β-Ta undergoes a phase transformation into α-Ta BCC structure, as identified by 6-fold symmetry in the electron diffraction pattern, with a ~2–5 nm thick amorphous interface between Cu–Ta. For FCC–BCC co-deposited Cu–Mo [11] and multilayer Cu–Nb [1] have both

shown Kurdjumov–Sachs (K–S) orientation relationship, $Cu_{(111)[110]}||Mo, Nb_{(110)[111]}$. Phase-separated regions in co-deposited Cu-α-Ta may organize into K–S, Nishiyama–Wassermann (NW), or a variant orientation relationship.

Although phase separation is significant, there are other factors that will influence microstructure morphologies, the most prominent of these other factors being the high internal (residual) stresses inherent to the nonequilibrium process of film deposition [22]. Although the growth stresses commonly encountered in low temperature deposition may be less significant than in elevated temperature deposition, heating and cooling during deposition induce internal stresses due to the coefficient of thermal expansion mismatch between the substrate and film materials. Applying the formula for biaxial strain and the coefficient of thermal expansion (CTE) for Cu of 16×10^{-6}, Ta of 6.5×10^{-6}, and Si of 2.6×10^{-6}, all in units of m/(m K), and known elastic constants, the calculated stress in a 50–50 at.% Cu–Ta film deposited at 800 °C is 60 MPa that will be compressive on heating during elevated temperature deposition and tensile on cooling to room temperature [23]. The resulting stresses in the films will affect the morphology of the Cu–Ta film microstructure that evolves during elevated temperature phase separation during co-deposition.

The objectives of this study are thus enumerated: determine the processing–microstructure relationship of PVD co-deposited Cu–Ta, characterize the microstructure and determine the phases present at multiple length scales with possible crystallographic orientation relationships, and develop an empirical understanding of the self-assembly mechanisms for future development of immiscible alloy systems with tailored mechanical performance.

Results

XRD characterization of crystal structure

All four deposited films depict prominent phase separation in the co-deposited Cu–Ta. Although the nominal composition of all the films was constant at 50–50 at.% Cu–Ta, as confirmed by X-ray fluorescence spectroscopy (XRF), the extent of phase separation and the phases present varied significantly across the 25, 400, 600, and 800 °C films, giving each a distinct microstructure morphology. X-ray diffraction (XRD) profiles for all four films are shown in Fig. 1. In the 25 °C film, one broad peak with low intensity was noted for 2θ from 33 to 39° which is consistent with nanocrystalline (002) and (410) β-Ta. A low intensity peak at 43° aligns with diffraction of the Cu(111) plane. This agrees with literature [24] that notes β-Ta as the preferred Ta phase for Ta films deposited at room temperature. As previously stated, β-Ta is a metastable state whose stability has previously been affiliated with the presence of oxygen during deposition. However, recent work has refuted

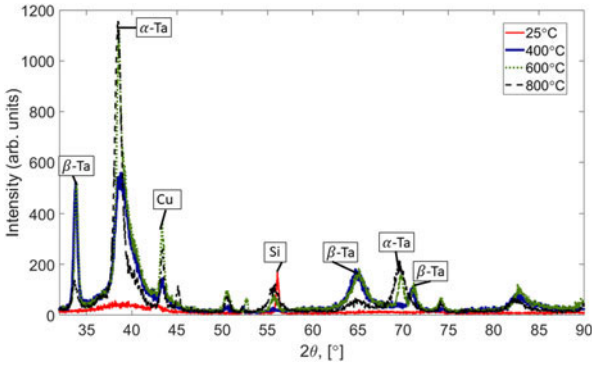

Figure 1: XRD spectra of the Cu–Ta films deposited at 25, 400, 600, and 800 °C. The 25 °C film has a broad peak with low intensity and a single sharp peak corresponding to Ta and Cu nanocrystals, respectively. The crystalline content of 400, 600, and 800 °C films greatly increases with high intensity peaks for planes Cu(111), β-Ta(110), and α-Ta(110) and others corresponding those three crystalline phases.

oxygen's stabilizing effect as β-Ta was observed in Ta depositions under ultrahigh vacuum [25]. The present work also employed high vacuum conditions, $<6 \times 10^{-7}$ Pa, which reduces the likelihood of oxygen contributing to β-Ta stability.

The crystalline peaks for β-Ta, α-Ta, and Cu were all present in the XRDs of the 400–800 °C films. The location and appearance of the β-Ta diffraction peaks agree with the tetragonal structure and lattice parameter spacings, *a*, *c*, first posed by Read and Altman [26] and later elaborated by Jiang et al. [27]. β-Ta (002) and higher index peaks sharply decline in intensity in the 800 °C films. α-Ta (110), $2\theta = 38°$ in Fig. 1, becomes increasingly prominent with increased deposition temperature, and the α-Ta (200) and (211) peaks also show increase in intensity in films deposited at 600 and 800 °C. The descent of the β-Ta and rise of the α-Ta peaks with increasing co-deposition temperature are consistent with other reports on structures of sputtered Ta thin films [21, 28]. In another study [28], the deposition was performed at room temperature that produced β-Ta structure, and β-Ta to α-Ta phase transformation was noted during postdeposition annealing at 750 °C [28]. The transformation was reported to occur at approximately 400 °C in the presence of Cu/Ta interfaces as previously noted in a study on Cu–Ta multilayers that were deposited at room temperature and annealed postdeposition [21]. In the present experiments, films were not annealed so it is unlikely if β-Ta to α-Ta phase transformation is involved, rather, the structure of the grains that nucleate during film growth depends on co-deposition temperature. The metastable and equilibrium phases of Ta will be further discussed later. Cu(111), (200), and (220) peaks were present and maintained the same or increasing intensity with respect to increasing deposition temperature suggesting a consistent FCC Cu presence for all films deposited at elevated temperatures.

STEM characterization of multiphase microstructure morphologies

Room temperature Co-deposition

Scanning/transmission electron microscopy (S/TEM) micrographs reveal the variant morphology of the four films. Figure 2 contains cross-sectional transmission electron microscopy (TEM) images of the film deposited at 25 °C. Energy-dispersive spectroscopy (EDS) X-ray mapping, Fig. 2(a), confirms the omnipresence of Cu and Ta across the film. High-resolution TEM (HR TEM), Fig. 2(b), images show adjacent nanocrystals of Cu and Ta with diameters on the order of ~5 nm homogenously distributed throughout the film. The selected area diffraction pattern (SADP), Fig. 2(c), of the room temperature film has diffuse concentric rings that align with Ta(110), (211), and Cu(111), respectively. Because the SADP corresponds to a cross-section TEM image, the uniform intensity in the diffraction rings does not indicate any strong texture. The nanocrystallinity is further supported by the Cu and broad β-Ta crystalline peaks in the XRD spectra of Fig. 1. Unlike the co-sputtered Cu–34 at.% Ta films reported in the literature [19], the room temperature of Cu–Ta film in this experiment did not exhibit any superlattice organization.

400 °C Co-deposition

Micrographs of the 400 °C film shown in Fig. 3 depict interwoven Cu-rich and Ta-rich regions that form a bicontinuous ribbon-like structure with wavy features oriented perpendicular to the growth direction. The morphology is reminiscent of the vertical concentration modulation (VCM) morphology reported for Cu–Mo [11] in the sense that the concentration modulation is approximately along the film growth (referred to as vertical) direction, but different since in Cu–Mo the VCM morphology resembled a multilayer structure but for Cu–Ta, Fig. 3, the morphology is interwoven with waviness amplitude larger than individual phase dimensions. STEM high-angle annular dark-field (HAADF) Z number contrast imaging, Fig. 3(a), confirms the wavy nature of the domains and that the average widths of the Ta-rich and Cu-rich bands are 124 ± 5 nm and 83 ± 4 nm, respectively. The Ta-rich bands are composed of nanocrystalline grains organized into columns approximately 15 nm in width that are elongated in the growth direction. Striations within the HR TEM image of Fig. 3(c) depicts planar defects present within the grains of Ta that are likely stacking faults that are generated to relax the high internal stresses that arise during film deposition [29]. It is also plausible the defects are nanoscale growth twins [30], but the resolution of the planar defects is distorted due to a lack of texture within the Ta columns and few Angstrom-scale spacing between planar defects. The planar faults in Ta thin films are typically associated with the β-Ta structure [24], but the crystallography and energetics of these defects are not understood, particularly the role of stress and impurities in sputtered Ta films that may exhibit planar defects in either β or α-Ta grains. HR TEM imaging, Fig. 3(d), within the Cu-rich bands shows that Cu maintains a semi-coherent boundary with the surrounding Ta. Examination of the phase separated interface and the inset fast Fourier transform (FFT) reveal a K–S orientation relationship at the semi-coherent boundary with $Cu\langle 10\bar{1}\rangle//Ta\langle 11\bar{1}\rangle$ and Cu (111)//Ta (011). Z-contrast imaging and HR TEM imaging reveals Ta nanocrystals present in limited areas within the Cu-rich bands. The ~4 nm in diameter Ta nanocrystals, exhibiting BCC structure, were likely precipitated via clustering of Ta atoms trapped in the Cu-rich domains during the deposition process. Conversely, there are Cu nanocrystals, ~5 nm in diameter, present in the Ta columnar grain as seen in Fig. 3(b) which are identified by FFT (inset) depicting an FCC crystalline structure. The presence of both Ta and Cu nanocrystals will be further explored in the following paragraphs as the feature fineness at 400 °C increased the difficulty for comprehensive characterization.

600 °C Co-deposition

Increasing the deposition temperature to 600 °C significantly altered the microstructure morphology. The substantial difference between the mobilities of Cu and Ta at 600 °C led to self-assembly of Cu into Cu-rich agglomerates spaced tens of microns apart, whereas Ta remained in Ta-rich vein-like structure either surrounding the islands or comprising the film between the Cu-rich agglomerates. Figure 4 portrays an overview of the film morphology along with HR TEM images for phase identification within the microstructure features. The self-assembly of Cu–Ta here is akin to that seen in Cu–Nb films which formed large spherulitic grains encompassed by an amorphous matrix [31]. As seen in Fig. 4(a), the Cu-rich islands, ranging from 30 to 500 nm in diameter, are composed of FCC Cu homogenously interspersed with fine Ta precipitates approximately 5 nm in diameter. Because of the relatively low mobility of Ta at 600 °C, the Ta adatoms landing within the Cu-rich agglomerates were able to diffuse small distances on the film surface before being trapped by the oncoming deposition layer. Figure 4(c) provides a HR TEM image of a Ta precipitate ~5 nm in diameter inside of a Cu-rich agglomerate, the FFT of the circled region (inset) aligns with a BCC α-Ta structure. The presence of Ta clusters in the Cu-rich agglomerates is reminiscent of 90–10 at.% Cu–Ta alloys formed with equal channel angular extrusion which developed Ta nanoclusters and particles within a Cu matrix due to severe plastic deformation [32]. The interface between the Cu-rich

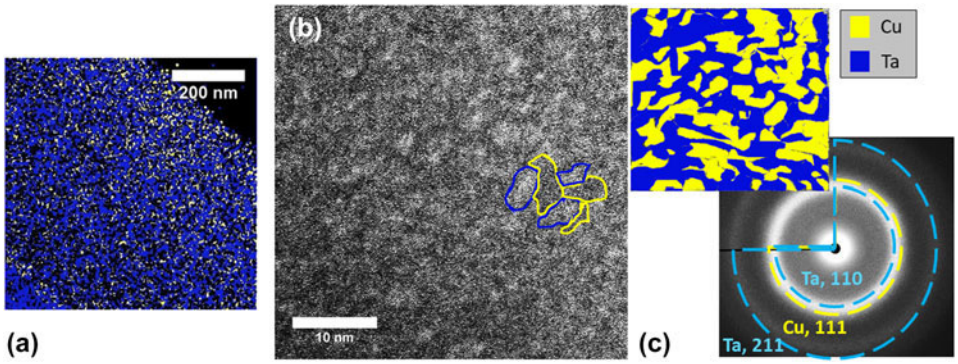

Figure 2: Characterization of film deposited at room temperature. (a) EDS X-ray map of homogenously distributed Cu–Ta nanocrystals, (b) HR TEM image of film cross section depicting fine nanocrystalline structure, a few nanocrystals are outlined in the image, (c) SADP of the same section and a cartoon schematic of microstructure colored to represent the phase region distribution in the microstructure.

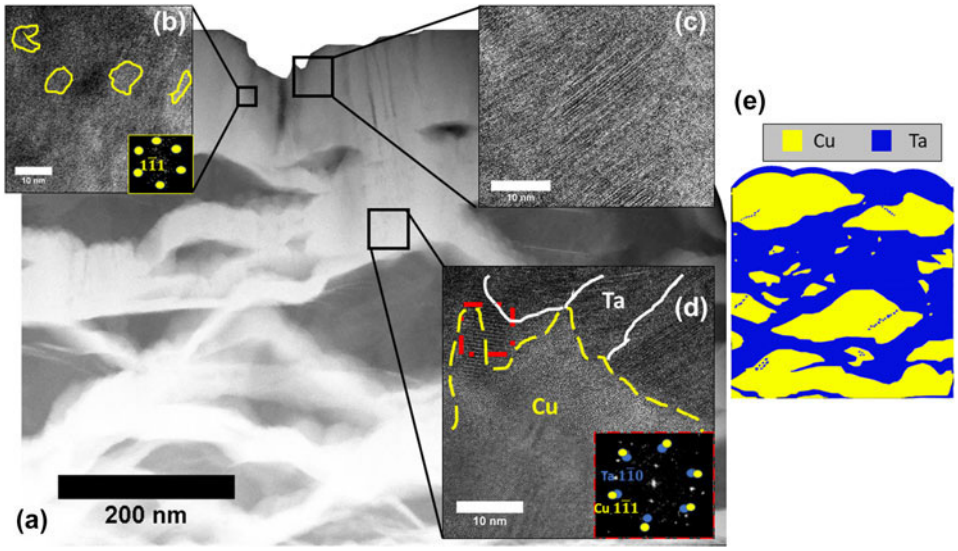

Figure 3: (a, background) STEM HAADF micrograph with atomic number contrast of Cu–Ta deposited at 400 °C. The white regions corresponding to Ta and darker regions are Cu bands. Within the Cu bands, trace Ta precipitates are noted. In the Ta-rich bands, Cu nanocrystals are present (b) as confirmed by HR TEM and FFT (inset) revealing a zone axis = $(1\bar{1}0)$ for an FCC Cu structure. (c) HR TEM in Ta-rich band showing planar defects aligned with angle to growth direction of film. (d) HR TEM of semi-coherent interface between Cu band and Ta band. FFT (inset) provides a K–S orientation relationship $Cu\langle 10\bar{1}\rangle//Ta\langle 11\bar{1}\rangle$ and Cu(111)//Ta(011). (e) Cartoon schematic of the microstructure.

agglomerates and the Ta-rich veins is clarified with HR TEM, Fig. 4 (b), that depicts semi-coherent boundary with a NW FCC–BCC orientation relationship $Cu\langle 0\bar{1}1\rangle//Ta\langle 001\rangle$ and $Cu(\bar{1}11)//Ta(\bar{1}10)$ which is just a 5.26° rotation from the K–S orientation relationship present in the 400 °C film. Within the Ta-rich veins, the nanocrystals arranged in columns elongated in the growth direction persist. Again, planar defects are noted as was the case in the 400 °C film. A key feature is a homogenous distribution of Cu nanocrystals present within the Ta-rich veins. Similar to those identified from Fig. 3(b), the Cu nanocrystals are small clusters of Cu adatoms that were buried during deposition and were unable to diffuse substantial distances to reach the larger Cu agglomerates due to limited bulk diffusivity as will be discussed further in this publication. The presence of features at two different length scales classifies this microstructure as a hierarchical structure. The first is microscale Cu-agglomeration and Ta-rich veins and the second being nanoscale Ta precipitates in the Cu-rich agglomerations and Cu nanocrystals in the Ta-rich veins. In the cross-sectional micrographs, the Cu-agglomerates account for just 33% of the area fraction which differs from the 50–50 at.% Cu–Ta of the XRF results. This suggests that approximately 17% of the Cu atoms in the thin film are present in the form of nanocrystalline precipitates within the Ta veins.

800 °C Co-deposition

As seen in Fig. 5(a), the final 800 °C film had a similar microstructure morphology as the 600 °C film with Cu-rich

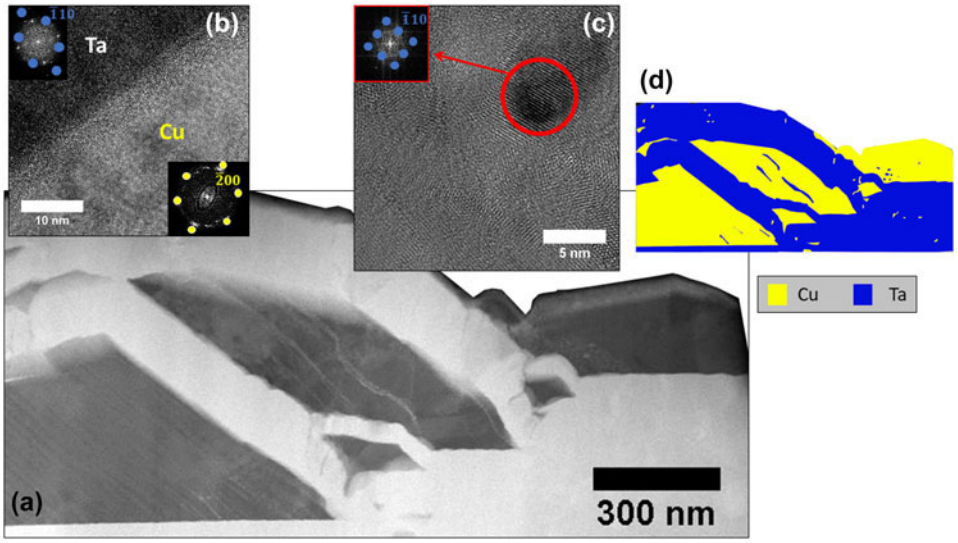

Figure 4: (a) STEM HAADF micrograph of Cu–Ta film deposited at 600 °C. White regions are Ta-rich veins and dark regions are Cu-rich agglomerates. (b) HR TEM image of the boundary between Ta veins and Cu agglomerates shows a semi-coherent interface with NW orientation relationship $Cu\langle 0\bar{1}1\rangle//Ta\langle 001\rangle$ and $Cu(\bar{1}11)//Ta(\bar{1}10)$ as confirmed by FFTs (inset). (c) HR TEM of a single Ta precipitate (encircled in red) in the Cu agglomerate, this is confirmed by FFT (inset) showing BCC Ta crystal, zone axis = $\langle 001\rangle$ (inset). (d) Cartoon schematic of microstructure.

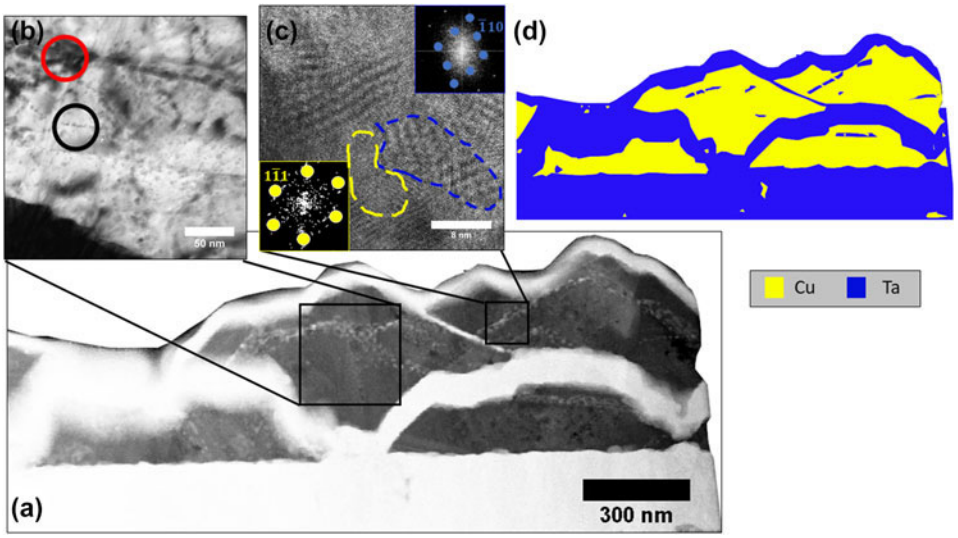

Figure 5: (a) STEM HAADF micrograph of Cu–Ta film deposited at 800 °C, white/lighter regions are Ta-rich veins and darker regions are Cu-rich agglomerates. (b) Brightfield (BF) TEM image to show dichotomy of Ta precipitates sizes present in the Cu-rich agglomerate, red circle shows precipitates ~10 nm in diameter, whereas black circle shows precipitates ~5 nm in diameter. (c) HR TEM micrograph of Ta precipitates within the Cu-rich agglomerate with a semi-coherent interface and NW orientation relationship $Cu\langle 0\bar{1}1\rangle//Ta\langle 001\rangle$ and $Cu(\bar{1}11)//Ta(\bar{1}10)$ as confirmed by FFTs (inset). Difference in lattice parameters [Ta (BCC) a = 3.3 pm and Cu a = 3.6 pm] is source of Moiré fringes. (d) Cartoon schematic of microstructure.

agglomerations enshrouded by Ta-rich veins and again having hierarchical microstructure features present on the micron and nanoscale. The key difference being the coarseness of microstructure features in both the Cu-rich and Ta-rich regions. The Ta-precipitates present in the Cu-rich agglomerates, Fig. 5(b), have a bimodal distribution with a first population of small Ta precipitates approximately 5 nm diameter; some interspersed randomly and others clustered along inhomogeneities such as dislocations within the Cu-rich islands. A second population of larger precipitates approximately 10 nm in diameter are heterogeneously distributed in the Cu-rich islands. Atomically resolved HR-STEM imaging and the associated FFT patterns of Fig. 5(c) depict that all Ta precipitates maintain a NW FCC–BCC orientation relationship with the Cu-rich agglomerate, $Cu\langle 0\bar{1}1\rangle//Ta\langle 001\rangle$ and $Cu(\bar{1}11)//Ta(\bar{1}10)$ and a semi-coherent boundary. The Ta-rich veins again contain the planar defects in their columnar grains as seen in the 400 and 600 °C films. The only difference is the limited presence of β-Ta at

800 °C, which further indicates that the Ta films may exhibit planar defects in either β or α-Ta grains. The interface between the Ta-rich veins and the Cu agglomerates has a semi-coherent boundary with the NW orientation relationship. Similar to the 600 °C film, there is a discrepancy in the Cu-rich area fraction being approximately 31% and the 50–50 at.% Cu–Ta confirmed via XRF. This suggests that approximately 19% of the Cu content in the thin film is embedded as nanocrystals within the Ta veins.

Stresses and macroscopic features

The residual stresses, as calculated from CTE mismatch, are 11 MPa, 45 MPa, and 60 MPa in the 400, 600, and 800 °C films, respectively, that will be compressive on heating (deposition temperature) and tensile on cooling. The internal stresses in the films are expected to play a role in determining the film morphology. Although the stress gradients have some influence on material flux, they play a more prominent role in the surface morphology of the Cu–Ta films which are characterized in a previous work by this author [33]. The combination of phase-separation and internal stresses lead to a morphologically rough surface in the 400 °C film. At higher deposition temperatures of 600 and 800 °C, the surface roughness is more pronounced with the appearance of grains protruding (that sometimes appear faceted) from the surface. During phase separation, there is an uneven coarsening with the Cu-rich agglomerates showing more coarsening as compared with Ta-rich regions, resulting in pronounced roughness with increasing temperature. Scanning electron microscopy (SEM) cross-sectional images in Fig. 6 reveal the wide variation in surface morphology with respect to deposition temperature.

The results of this experiment showed that Cu–Ta film morphology varied as a direct function of deposition temperature. As the deposition temperature increased, the film microstructure evolved from phase separated nanocrystals to a wavy structure with concentration modulations approximately along the film growth direction to hierarchical structures of Cu-rich agglomerations surrounded by Ta-rich veins. In the 600 and 800 °C case, Ta precipitates were noted within the Cu-rich islands and Cu nanocrystals were present within the Ta-rich veins. The cross-sectional SEM images of Fig. 6 provide a macroscopic view of the film cross-sections. The Cu–Ta maintains a bicontinuous structure in the 400 °C film. Although the 600 and 800 °C films both depict Cu-rich agglomerations, the agglomerates are spaced further apart separated by large sections of predominantly Ta-rich veins in the 600 °C film in contrast to the 800 °C film which maintains a closer spatial distribution of the agglomerates. This research used changes in deposition temperature to influence the kinetics of phase separation during deposition. Other important factors such as deposition rate, chamber pressure, inert gas pressure, and energy of the oncoming adatoms could all be varied and are worthy of future inspection as they may yield interesting microstructural results.

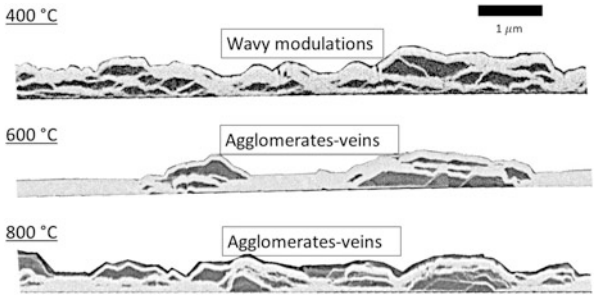

Figure 6: Backscattered electron (BSE) SEM images of 400, 600, and 800 °C film cross sections. The white regions are Ta-rich, and the dark regions are Cu-rich.

Discussion

Microstructural analysis

The positive enthalpy of mixing, and differences in atomic size and crystal structure induced phase separation between Cu and Ta regions. The self-assembled phase-separated microstructure of these co-deposited Cu–Ta heterogeneous thin films maintains moderate qualitative agreement with literature results. XRD results from PVD co-deposited Cu–Ta films by Muller et al. [18] depict amorphous as-deposited samples that crystallize into FCC–Cu and β-Ta after annealing at 600 and 800 °C. Nastasi et al. [34] annealed electron beam deposited 50–50 at.% Cu–Ta films and reported similar initially amorphous as-deposited samples. On the contrary, the 25 °C film in this experiment was nanocrystalline as evidenced by the broadened XRD crystalline peaks for Cu(111) and β-Ta(200), Fig. 1, and HR TEM and SADP of Fig. 2. The presence of crystallinity, compared with its absence in the two literature cases, can be explained by the significantly lower deposition rate of the co-deposition which gives the adatoms sufficient time to diffuse and form nanocrystals before being arrested by the subsequent layer despite their relatively low kinetic energy. The kinetics and thermodynamics of PVD co-deposition will be further explained in this section.

The results of this experiment show a continuous evolution of film microstructure morphology as the deposition temperature increases from 400 to 800 °C. Cu–Ta films in the literature depict an increase in crystalline character after annealing with larger Ta grains and Cu forming interwoven clusters throughout the sample bulk [18, 19]. In this work, the microstructures of the 400–800 °C films follow the same crystallization trend but differ greatly in morphology. The wavy morphology of the 400 °C film with concentration

modulation along film growth direction is akin to that observed in co-deposited Cu–Mo [11] and sputtered Cu–W both at 400 °C [4]. The Cu-rich agglomerations surrounded by Ta-rich bands along with features on different length scales in the 600 and 800 °C films align with the hierarchical microstructures of Cu–Mo [12] which formed macroscale Cu–Mo modulations along with Cu-rich islands containing nanoscale Mo precipitates. The Mo precipitates were either the BCC or FCC crystal structure depending on the precipitate's size that influenced its susceptibility toward mismatch strain relative to the surrounding Cu FCC lattice. Thus, Mo was either strained to form a coherent interface or formed a semi-coherent interface with a K–S orientation relationship to Cu. For the Ta precipitates within the 600 and 800 °C Cu–Ta films, Ta maintained its BCC structure and NW orientation relationship with the surrounding FCC Cu-rich agglomerate. This suggests that although co-deposited immiscible elements can self-organize into hierarchical morphologies metastable crystal structures may form in some but not in others. In Cu–Mo, the nanoscale clusters of Mo atoms in Cu grains exhibited FCC structures, but in this study, Ta nanocrystals were BCC.

The results of this experimental study show three microstructure trends that correlate to increasing deposition temperature. First, increased deposition temperatures result in coarser Cu and Ta grains. Second, the crystal structure of the Ta grains depends on deposition temperature: β-Ta structure at the room temperature and α-Ta structure at 800 °C. (discussed further later in this section). At intermediate temperatures (400 °C and 600 °C), some grains exhibited β-Ta structure, whereas others had α-Ta structure, with the fraction of the latter increasing with increasing deposition temperature. No evidence of phase transformation from β-Ta to α-Ta was observed during deposition, and the deposited films were not annealed postdeposition. Third, the evolution of the microstructure with increasing temperature from nanocrystalline to wavy-VCM structure to agglomerate-vein structure with hierarchical features depicts a novel processing–microstructure relationship for PVD co-deposited Cu–Ta films.

Phase separation phenomena

Multiple competing internal forces influence the movement of species during deposition of a co-sputtered metallic thin film. The complex relationship of PVD kinetics and thermodynamics gives rise to metastable states and nonequilibrium microstructures in the resulting metallic films as noted in past literature cases [11, 12, 18, 35]. In this experiment, Cu and Ta adatoms landing on the substrate surface will diffuse with respect to chemical potential and stress gradients into phase-separated regions due to immiscibility at the deposition temperatures. The adatoms will move a limited distance on the film surface before being buried by the oncoming deposition layer and be essentially frozen into place as their bulk diffusivity is orders of magnitude lower than their surface diffusivity. For example, in the self-diffusion of Cu, the bulk diffusivity is 3.8×10^{-6} m^2/s versus the surface diffusivity of 2.5×10^{-4} m^2/s at 500 °C [36]. Depositions at relatively low homologous temperatures have been treated in the literature under the "frozen bulk approximation" [37]. Thus, the surface diffusion is the dominant kinetic process during thin film growth at low homologous temperatures, and is controlled by the deposition rate, which determines the time between consecutive oncoming layers, and by the deposition temperature which is directly proportional to diffusivity.

Prior research related the spacing of phase-separated regions in PVD immiscible alloy systems to calculated surface diffusion distances [33, 35]. Although valid, surface diffusion distances cannot fully explain the agglomeration and precipitate formation seen in Cu–Ta deposited at 600 and 800 °C. Instead, an empirical understanding of these features is best formed by evaluating the mobilities of the constituent species at the various deposition temperatures. Direct comparison of the mobility will provide perspective of how one element may move relative to the other. Work by Fukutani et al. [38] uses a mobility-dependent Cahn–Hilliard expression to describe an Al–Si thin film system that readily phase separates during growth via spinodal decomposition with the separation limited to the growth surface. The similarities between the Al–Si system and the present work allow for an adaptation of the mobility expression to examine the Cu–Ta microstructures. Mobility is defined as:

$$M = \frac{D \times c_0(1 - c_0)}{k_b T} \quad , \tag{1}$$

where M is the mobility, c_0 is the overall composition of one component, k_b is Boltzmann's constant, T is the deposition temperature, and D is the diffusivity of the species which is in turn solved with the well-known expression [39]:

$$D = D_0 \exp\left(\frac{-Q}{k_b T}\right) \quad , \tag{2}$$

with D_0 as a diffusivity coefficient, Q is the activation energy required for the movement of an atom to an available adjacent site. As surface diffusion is dominant, the surface diffusion values for D_0 and Q are selected for each species. The mobility is defined as a velocity of particles per unit of force and in the case of Cu–Ta film growth, the force is the phase-separating driving force. The units are cm^2/(s/eV). Similar mobility arguments have been used in phase field models describing phase separation into modular systems. These phase field models have been successful in replicating the VCM-like structure seen in the 400 °C film of this experiment [14, 40].

From Eq. (2), the mobility of the Cu and Ta adatoms plotted as a function of deposition temperature in Fig. 7 depicts a high mobility of Cu compared with the relatively immobile Ta at 25, 400, 600, and 800 °C. With such low mobility values, the Ta adatoms are essentially frozen once they land on the surface. At 25 °C both Cu and Ta are immobile with limited diffusion which accounts for the ~5 nm diameter nanocrystalline structure of the relevant film. For the 400, 600, and 800 °C films, the highly mobile Cu adatoms perform the majority of the material diffusion for the phase separation during deposition. With moderately high mobility, the Cu moves to form the VCM-like structure of the 400 °C film. In the 600 and 800 °C films, the Cu has with significantly elevated mobility which, paired with the low deposition rate of 1.52 Å/s that provides ample time for surface diffusion before burial by the subsequent depositing layer, enabled Cu agglomeration. The Ta precipitates are formed by immobile Ta adatoms trapped within the Cu grains. The Ta is capable of small-scale diffusion at elevated temperatures and thus clustered into precipitates before being enveloped by the Cu. While most Cu adatoms landing on the surface of Ta-rich veins moved to form the Cu-rich sections, some Cu adatoms were trapped and surrounded by the Ta to form the small Cu nanocrystals seen inside the columnar grains of the Ta-rich veins.

The mobility argument explains the difference between the Cu–Ta microstructures of this work and those of Muller et al. [18, 19]. In Muller et al., the Cu–Ta is deposited at room temperature where both species have low mobilities. The samples were annealed to enable coarsening via bulk diffusion and formation of tortuous Cu-rich regions along with large Ta grains. In the present research, the co-deposition of Cu–Ta at elevated temperatures, where Cu is significantly more mobile than the higher melting point Ta, accentuates the disparity of the constituent element mobilities leading to the entrapment of Ta as precipitates within the Cu-rich regions and the Cu clusters within the Ta-rich veins.

Metastable states

It is worthwhile to discuss the crystal structure of Ta as a function of increasing deposition temperature. In the case of immiscible Cu–Nb systems, nanoscale phase separation reduces the free energy and incentivizes the metastable amorphous phase [41]. The crystal structure of the grains is determined by the thermodynamic driving forces and the surface energy of the phases as they nucleate and grow during deposition. As seen in Figs. 2–5, the Ta adatoms are not landing on a coherent crystal lattice but rather a series of nanocrystals or clusters with a variety of orientations. Therefore, the system can be represented as Ta crystals growing on an amorphous substrate. Classical nucleation theory can be used to express the nucleation rate as:

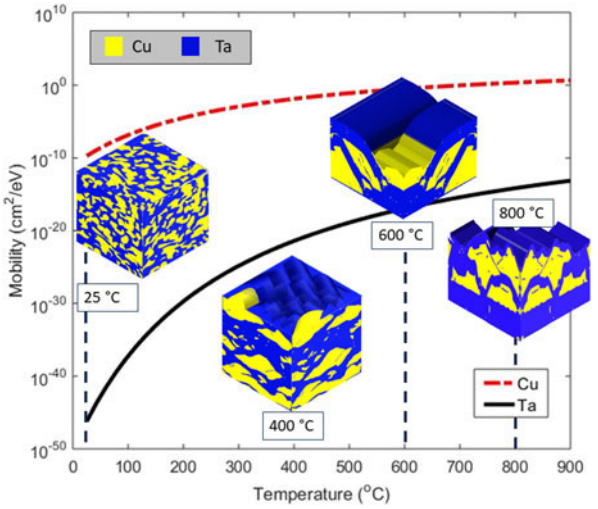

Figure 7: Mobility of the constituent Cu and Ta adatoms as a function of temperature during PVD. (Inset) Cartoon schematics of the film morphologies at the respective temperatures (constant deposition rate, 1.52 Å/s for all).

$$R \propto \exp\left(\frac{-E_1}{kT}\right)\exp\left(\frac{-W^*}{kT}\right) \quad , \tag{3}$$

Where the nucleation rate, R, is proportional to the exponential of the activation energy for adatoms to diffuse to the nuclei, E_1, Boltzmann's constant, k, temperature, T, and the nucleation barrier related to Gibbs free energy, W^*. The nucleation barrier is expressed as:

$$W^* = \frac{1}{3}\pi\left[\frac{\left(\Delta\gamma_{a-c}^{\text{interface}} + 2\Delta\gamma_{a-c}^{\text{surface}}\right)}{\left(\Delta g_{a-c}^{\text{Ta}}\right)}\right] \quad . \tag{4}$$

The $\Delta\gamma_{a-c}^{\text{interface}}$ is the change in interfacial energy and $\Delta\gamma_{a-c}^{\text{surface}}$ is the change in surface energy of the growing crystal nuclei on the amorphous substrate. The change in Gibbs free energy, $\Delta g_{a-c}^{\text{Ta}}$, acts as the driving force for chemical growth. The expression for the nucleation barrier and the W^* notation is derived from the change in Gibbs free energy of formation at a critical nuclei radius, r^*.

Further details on the thermodynamic quantities, including the exact values of changes in Gibbs free energy and surface energies, are available in Colin et al. [25]. More importantly, the qualitative understanding is that the change in Gibbs free energy is larger for α-Ta than for β-Ta crystalline formation at room temperature. Although this would normally prefer α-Ta nucleation rather than β-Ta, the surface energy provides a significant contribution to the overall free energy with $\Delta\gamma_{a-\alpha}^{\text{surface}} > \Delta\gamma_{a-\beta}^{\text{surface}}$. Factoring in the surface energy difference and change in Gibbs free energy into Eq. (3) explains a preference for β-Ta nucleation and prevalence of β-Ta in the films deposited at temperatures ≤400 °C. In addition, film

growth residual stresses in these low temperature films may induce the Ta crystallites to tetragonally distort into the β-Ta structure. Beyond 400 °C, the energy barrier for homogenous nucleation of the β-Ta exceeds that of α-Ta, $W_{\beta}^{*} > W_{\alpha}^{*}$, leading to the preferred nucleation of α-Ta as seen from Eq. (4). On a final point, the phase separation of Cu and Ta will induce spatial heterogeneity in the interfacial energy term in the classical nucleation theory. In addition, strain energy in the film due to film growth residual stresses at low temperatures could contribute to a nonuniform Ta crystal structure. Both may have caused differences in preferred phase of Ta nucleation at different locations in the film within a constant deposition temperature.

Conclusions

The elevated temperature co-sputtering of Cu–Ta yielded four unique microstructures that were previously unobserved in phase-separated FCC–BCC thin films. As the deposition temperature increased from 25 to 800 °C, the microstructure varied from nanocrystals to a wave-like vertical concentration modulated structure to Cu-rich agglomerations and Ta-rich veins with hierarchical features. The multimodal (hierarchical) structure is particularly pervasive in the 600 and 800 °C films. At the macroscale, the Cu and Ta organize into Cu-rich agglomerates and Ta-rich veins. At the nanoscale, examination of the Cu-rich agglomerates revealed a number of enclosed Ta precipitates, whereas inspection of the Ta-rich veins showed small Cu nanocrystals entrapped within the Ta columnar grains. Prominent phase separation occurred for all deposition temperatures, and in the 400, 600, and 800 °C cases, semi-coherent boundaries were noted between the Cu-rich and Ta-rich regions. Two common orientation relationships, NW and K–S, were noted either between the Cu-rich agglomerations and Ta-rich veins or at the nanoscale with Ta precipitates enclosed in the Cu-rich clusters. Significant internal stresses paired with phase-separation phenomena at the elevated deposition temperatures 400, 600, and 800 °C, caused roughened features and/or protruding grains on the film surfaces.

The various microstructures are the result of a large difference in constituent element mobility at the experimental film deposition temperatures. As the mobility of Cu is of orders of magnitude higher than that of Ta, the resultant microstructures are chiefly the product of highly mobile Cu and relatively immobile Ta. Both species migrate via surface diffusion when depositing flux arrives on the substrate, but when buried in the bulk after the next layer gets deposited, Cu may have significant bulk diffusivity, whereas Ta will have negligible bulk diffusivity at the deposition temperatures used in these experiments. XRD and S/TEM micrographs have revealed equilibrium and metastable states of Cu and Ta: FCC Cu, α-Ta (BCC), β-Ta (tetragonal). Their presence is reasoned by changes in Gibbs free energy and interfacial energy, which act as driving forces for phase organization. Future work will examine the mechanical performance of these microstructures which should yield interesting results due to the complex interfaces at a variety of length scales and the influence they will have on dislocation motion and plastic deformation.

Methods

Cu–Ta thin films were co-deposited via the PVD process of DC magnetron sputtering using a pressure chamber with a base pressure $<6 \times 10^{-7}$ Pa. The Cu and Ta targets were simultaneously activated to co-deposit a film with 50–50 at.% Cu–Ta composition onto Si–SiO_2 substrates with millimeter thickness. The top 1000 nm of the substrate, contacting the film surface, is SiO_2, whereas the remainder is Si. The 50 at.% was selected to focus on bicontinuous morphologies rather than minority phase segregation of either element. The deposition chamber was a Kurt Lesker PVD 75 with 2″ disk Cu and Ta targets with nominal purities of 99.999% for Cu and 99.95% for Ta with a target throw distance of 5″. The substrates were cleaned with an RF bias of 50 W for 120 s before deposition. Cu–Ta films were deposited at a combined co-deposition rate of 1.52 Å/s to 700 nm thickness at four temperatures: 25 (room temperature), 400, 600, and 800 °C. The deposition temperature refers to the temperature of the substrate that is heated via a heating coil to a consistent temperature during the deposition. All the films were deposited and then left to cool to room temperature in the deposition chamber to prevent oxide formation on the film surface.

The bulk composition of the alloy films was confirmed via XRF using a Rigaku Supermini200. To ensure accurate composition, targeted scans in the keV energy ranges for the Cu Lβ and Ta Mα peaks were performed in addition to a general sweep of metallic element peaks. Therefore, each film was scanned a total of eight times with Gaussian peak fits applied to reduce noise. The average standard deviation in composition was <3.5 at.%. XRD with a Rigaku SmartLab XRD with a Cu source (λ = 1.54 Å) was used to determine the phase composition of the four samples. An initial XRD scan was run continuously at 2θ range from 10° to 90° with a speed of 4°/s and a step size of 0.02°. To increase data resolution, a second detailed scan was run at 2θ from 32° to 52° with s scanning speed of 1°/s and a step size of 0.005°.

S/TEM cross-sectional samples of the film were prepared using focused ion beam milling techniques in a FEI Helios 650 nanolab SEM/FIB. The foils were attached to Mo grids to minimize any interference to compositional mapping. Transmission electron microscopy was performed with a JEOL

2010F AEM with 200 kV voltage. Two scanning transmission electron microscopes, JEOL 2100F STEM and JEOL 200 C-ARM, operated at 200 keV using Gatan and JEOL detectors were used for high-resolution characterization of film cross-sectional samples. EDS on the JEOL 200 C-ARM was used for compositional spatial mapping of the samples.

Acknowledgments

This research was performed under the Center for Research Excellence on Dynamically Deformed Solids (CREDDS) sponsored by the Department of Energy—National Nuclear Security Administration (DOE-NNSA), Stewardship Science Academic Program under the Award No. DE-NA0003857.

Microscopy was performed at the Michigan Center for Materials Characterization at the University of Michigan (JEOL 2010F AEM and JEOL 2100F STEM). Some of the high-resolution S/TEM characterization (JEOL 200 C-ARM) was performed at Northwestern University under the Northwestern University Atomic and Nanoscale Characterization Experimental Center in the Electron Probe Instrumentation Center assisted by Dr. Xiaobing Hu and Dr. Kun He.

References

1. **J. Avallone, T. Nizolek, T. Pollock, and M. Begley**: A model for high temperature deformation of nanolaminate Cu–Nb composites. *Mater. Sci. Eng., A* **761**, 138016 (2019).
2. **K. Wu, J. Zhang, J. Li, Y. Wang, G. Liu, and J. Sun**: Length-scale-dependent cracking and buckling behaviors of nanostructured Cu/Cr multilayer films on compliant substrates. *Acta Mater.* **100**, 344–358 (2015).
3. **Y. Cui, B. Derby, N. Li, and A. Misra**: Design of bicontinuous metallic nanocomposites for high-strength and plasticity. *Mater. Des.* **166**, 107602 (2019).
4. **F.T.N. Vullers and R. Spolenak**: From solid solutions to fully phase separated interpenetrating networks in sputter deposited "immiscible" W–Cu thin films. *Acta Mater.* **99**, 213–227 (2015).
5. **Y. Cui, N. Li, and A. Misra**: An overview of interface-dominated deformation mechanisms in metallic nanocomposites elucidates using in situ straining in a TEM. *J. Mater. Res.* **34**, 1470–1478 (2019).
6. **N. Mara and I. Beyerlin**: Interface-dominant multilayers fabricated by severe plastic deformation: Stability under extreme conditions. *Curr. Opin. Solid State Mater. Sci.* **19**, 265–276 (2015).
7. **A. Misra, M. Demkowicz, X. Zhang, and R. Hoagland**: The radiation damage tolerance of ultra-high strength nanolayered composites. *JOM* **59**, 62–65 (2007).
8. **Y.C. Wang, A. Misra, and R. Hoagland**: Fatigue properties of nanoscale Cu/Nb multilayers. *Scripta Mater.* **54**, 1593–1598 (2006).
9. **I. Beyerlin and J. Wang**: Interface-drive mechanisms in cubic/noncubic nanolaminates at different scales. *MRS Bull.* **44**, 31–39 (2019).
10. **J. Thornton**: Influence of apparatus geometry and deposition conditions on the structure and topography of thick sputtered coatings. *J. Vac. Sci. Tech.* **11**, 666–670 (1974).
11. **B. Derby, Y. Cui, J.K. Baldwin, and A. Misra**: Effects of substrate temperature and deposition rate on the phase separated morphology of co-sputtered Cu–Mo thin films. *Thin Solid Films* **647**, 50–56 (2018).
12. **B. Derby, Y. Cui, J.K. Baldwin, R. Arroyave, M. Demkowicz, and A. Misra**: Processing of novel psuedomorphic Cu–Mo hierarchies in thin films. *Mater. Res. Lett.* **7**, 1–11 (2019).
13. **Y. Lu, C. Wang, Y. Gao, R. Shi, X. Liu, and Y. Wang**: Microstructure map for self-organized phase separation during film deposition. *Phys. Rev. Lett.* **109**, 086101 (2012).
14. **A. Kumar, B. Derby, R. Raghavan, A. Misra, and M. Demkowicz**: 3-D phase-field simulations of self-organized composite morphologies in physical vapor deposited phase-separating binary alloys. *J. Appl. Phys* **126**, 075306 (2019).
15. **K. Holloway, P. Fryer, C. Cabral, J.M.E. Harper, P.J. Bailer, and K.H. Kelleher**: Tantalum as a diffusion barrier between copper and silicon: Failure mechanism and effect of nitrogen additions. *J. Appl. Phys* **71**, 5433 (1992).
16. **A. Jain, S.P. Ong, G. Hautier, W. Chen, W.D. Richards, S. Dacek, S. Cholia, D. Gunter, D. Skinner, G. Ceder, and K.A. Persson**: The materials project: A materials genome approach to accelerating materials innovation. *APL Mater.* **1**, 011002 (2013).
17. **M. Buehler and A. Misra**: Mechanical behavior of nanocomposites. *MRS Bull.* **44**, 19–24 (2019).
18. **C.M. Muller, S. Parviainen, F. Djurabekova, K. Nordlund, and R. Spolenak**: The as-deposited structure of co-sputtered Cu–Ta alloys, studied by X-ray diffraction and molecular dynamics simulations. *Acta Mater.* **82**, 51–63 (2015).
19. **C.M. Muller, A. Sologubenko, S. Gerstl, and R. Spolenak**: On spinodal decomposition in Cu-34 at.% Ta thin films—An atom probe tomography and transmission electron microscopy study. *Acta Mater.* **89**, 181–192 (2015).
20. **K.W. Kwon, C. Ryu, R. Sinclair, and S.S. Wong**: Evidence of heteroepitaxial growth of copper on beta-tantalum. *Appl. Phys. Lett.* **71**, 3069 (1997).
21. **H.J. Lee, K.W. Kwon, C. Ryu, and R. Sinclair**: Thermal stability of a Cu/Ta multilayer: An intriguing interfacial reaction. *Acta Mater.* **47**, 3965–3975 (1999).
22. **M. Jackson and C. Li**: Stress relaxation and hillock growth in thin films. *Acta Metall.* **30**, 1993–2000 (1982).
23. **A. Segmuller and M. Murakami**: X-ray diffraction analysis of strains and stresses in thin films. *Treatise Mater. Sci. Technol.* **27**, 143–200 (1988).
24. **A. Jiang, T.A. Tyson, L. Axe, L. Gladczuk, M. Sosnowski, and P. Cote**: The structure and stability of β-Ta thin films. *Thin Solid Films* **479**, 166–173 (2005).
25. **J.J. Colin, G. Abadias, A. Michel, and C. Jaouen**: On the origin of the metastable β-Ta phase stabilization in sputtered thin films. *Acta Mater.* **126**, 481–493 (2017).

26. **M. Read and C. Altman**: A new structure in tantalum thin films. *Appl. Phys. Lett.* **7**, 51 (1965).
27. **A. Jiang, A. Yohannan, N. Nnolim, T.A. Tyson, L. Axe, S. Lee, and P. Cote**: Investigation of the structure of β-Ta. *Thin Solid Films* **437**, 116–122 (2003).
28. **S.L. Lee, M. Doxbeck, J. Mueller, M. Cipollo, and P. Cote**: Texture, structure, and phase transformation in sputter beta tantalum coating. *Surf. Coating. Technol.* **177–178**, 44–51 (2004).
29. **L.A. Clevenger, A. Mutscheller, J.M.E. Harper, C. Cabral, and K. Barmak**: The relationship between deposition conditions, the beta to alpha phase transformation, and stress relaxation in tantalum thin films. *J. Appl. Phys.* **72**, 4918 (1992).
30. **J. Wang and X. Zhang**: Twinning effects on strength and plasticity of metallic materials. *MRS Bull.* **41**, 274–281 (2016).
31. **A. Puthucode, A. Devaraj, S. Nag, S. Bose, P. Ayyub, M.J. Kaufman, and R. Banerjee**: De-vitrification of nanoscale phase-separated amorphous thin films in the immiscible copper-niobium system. *Phil. Mag.* **94**, 1622–1641 (2014).
32. **M. Rajagopalan, K. Darling, S. Turnage, R.K. Koju, B. Hornbuckle, Y. Mishin, and K.N. Solanki**: Microstructural evolution in a nanocrystalline Cu–Ta alloy: A combined in situ TEM and atomistic study. *Mater. Des.* **113**, 178–185 (2017).
33. **M. Powers, B. Derby, E. Raeker, N. Champion, and A. Misra**: Hillock formation in co-deposited thin films of immiscible metal alloy systems. *Thin Solid Films* **693**, 137692 (2020).
34. **M. Nastasi, F.W. Saris, L.S. Hung, and J.W. Mayer**: Stability of amorphous Cu/Ta and Cu/W alloys. *J. Appl. Phys.* **58**, 3052–3058 (1985).
35. **J. Xue, Y. Li, L. Hao, L. Gao, D. Qian, Z. Song, and J. Chen**: Investigation on the interfacial stability of multilayered Cu–W films at elevated deposition temperatures during co-sputtering. *Vacuum* **166**, 162–169 (2019).
36. **H.P. Bonzel: Surface diffusion tables.** In *Diffusion in Solid Metals and Alloys*, 1st ed., H. Mehrer, ed. (Springer-Verlag, Berlin, Germany, 1990); pp. 728–744.
37. **C.D. Adams, M. Atzmon, Y.T. Cheng, and D.J. Srolovitz**: Phase separation during co-deposition of Al–Ge thin films. *J. Mater. Res.* **7**, 653–666 (1991).
38. **K. Fukutani, K. Tanji, T. Saito, and T. Den**: Fabrication of well-aligned Al nanowire array embedded in Si matrix using limited spinodal decomposition. *Jpn. J. Appl. Phys.* **47**, 1140–1146 (2008).
39. **M. Ohring**: *Materials Science of Thin Films: Deposition and Structure*, 2nd ed. (Academic Press, San Diego, 2002); p. 495.
40. **J. Stewart and R. Dingreville**: Microstructure morphology and concentration modulation of nanocomposite thin-films during simulation physical vapor deposition. *Acta Mater.* **188**, 181–191 (2020).
41. **R. Banerjee, A. Puthucode, S. Bose, and P. Ayyub**: Nanoscale phase separation in amorphous immiscible copper-niobium alloy thin films. *Appl. Phys. Lett.* **90**, 021904 (2007).